

# The origin of the X-ray emission from the non-starburst gas-rich luminous infrared galaxies Arp 302

Jiachen Jiang,<sup>1\*</sup> William Baker,<sup>2,3</sup> Andrew Young<sup>4</sup> and Luigi Gallo<sup>5</sup>

<sup>1</sup>*Institute of Astronomy, University of Cambridge, Madingley Road, Cambridge CB3 0HA, UK*

<sup>2</sup>*Cavendish Laboratory – Astrophysics Group, University of Cambridge, 19 JJ Thomson Avenue, Cambridge CB3 0HE, UK*

<sup>3</sup>*Kavli Institute for Cosmology, University of Cambridge, Madingley Road, Cambridge CB3 0HA, UK*

<sup>4</sup>*School of Physics, Tyndall Avenue, University of Bristol, Bristol BS8 1TH, UK*

<sup>5</sup>*Department of Astronomy and Physics, Saint Mary's University, 923 Robie Street, Halifax, NS, B3H 3C3, Canada*

Accepted XXX. Received YYY; in original form ZZZ

## ABSTRACT

We present an analysis of the *XMM-Newton* observation of luminous infrared merging galaxies Arp 302 and a joint re-analysis of its *Chandra* observation. In particular, we focus on the more significant X-ray emitter of the pair, Arp 302N. *Chandra* detects significant soft X-ray emission from the hot gas in the star-forming region of Arp 302N spreading up to 12 kpc. We estimate the star-formation rate of Arp 302N to be around 1–2  $M_{\odot} \text{ yr}^{-1}$  based on the X-ray luminosity of the star-forming region, similar to previous measurements at longer wavelengths. *Chandra* and *XMM-Newton* observations show evidence of a Si XIII emission line with 86% confidence. Our best-fit model infers a super-solar silicon abundance in the star-forming region, likely related to the past core-collapse supernovae in this galaxy. Similar silicon overabundance was reported in the circumstellar medium of core-collapse supernova remnants in our Galaxy.

We also detect narrow Fe K $\alpha$  and Fe K $\beta$  (98.6% confidence) emission lines as part of the AGN emission. Our best-fit spectral model using *mytorus* indicates the evidence of a heavily obscured power-law emission with  $N_{\text{H}} > 3 \times 10^{24} \text{ cm}^{-2}$  in addition to a weak, unobscured power-law emission. The scattering fraction of the unobscured power-law emission from Compton-thin materials is 0.7%. All these spectral features suggest evidence of a Seyfert 2-like AGN in Arp 302N. The X-ray measurement of its AGN activity is consistent with the previous *Spitzer* measurement of the same object.

**Key words:** galaxies: star formation; X-rays: galaxies; galaxies: active

## 1 INTRODUCTION

Luminous infrared galaxies (LIRGs) have a high infrared luminosity of  $L_{\text{IR}, 8-1000\mu\text{m}} > 10^{11} L_{\odot}$  (e.g., Pérez-Torres et al. 2021). Many of them are believed to be powered by star-formation and/or an active galactic nucleus (AGN, e.g. Sanders & Mirabel 1996; Pérez-Torres et al. 2021). Observations and theoretical studies suggest that mergers may be the driving mechanism, lead to star formation and possibly fuel the AGN (e.g., Clements et al. 1996; Hopkins et al. 2006; Yuan et al. 2010; Kawaguchi et al. 2020; Ricci et al. 2023). The likely mechanism for the enhanced infrared luminosity is massive stars and/or AGN emitting ultraviolet photons, which heat a large amount of dust and gas in the galaxy, resulting in the strong infrared emission (Stierwalt et al. 2013). Therefore, gas-rich galaxy mergers are considered a key stepping stone to the understanding of the coevolution of galaxies and their central supermassive black holes (SMBHs, Hopkins et al. 2006; Zhuang & Ho 2023). A sustainable supply of gas-rich galaxy mergers would fuel their galaxy

and SMBH coevolution, whereby giant molecular clouds could get funnelled towards the central region by the effects of dynamical friction (boosting growth, Lin et al. 2023), whilst AGN activity caused by the supply of gas regulates the process (Liao et al. 2023).

A specific subgroup of infrared galaxies is called ultra-luminous infrared galaxies (ULIRGs) and have an even higher luminosity  $L_{\text{IR}} > 10^{12} L_{\odot}$ . These could likely have once been ordinary LIRGs boosted by mergers (Stierwalt et al. 2013). In addition, recent evidence has been found for a dual AGN fraction of at least 5% in a sample of local ULIRGs (Efstathiou et al. 2022).

The study of the circumnuclear environments of the accreting SMBHs in ULIRGs is difficult due to gas and dust obscuration. X-rays, especially hard X-rays less affected by obscuration, become a powerful tool to probe their hidden AGNs. For instance, Yamada et al. (2021) leveraged all archival X-ray data from *Chandra*, *XMM-Newton*, *Suzaku*, *NuSTAR* and *Swift* of the *Swift*-BAT LIRGs and ULIRGs and found a high fraction of Compton-thick absorption in both late and early mergers, 25% and 65% respectively. A similar conclusion was drawn by an earlier piece of work in Ricci et al. (2017). The young population of the binary system, e.g., high-mass

\* E-mail: jj447@cam.ac.uk

X-ray binaries (HMXBs) and supernova remnants, O-type stars in the star-forming region of these infrared galaxies, also produce a lot of emission in the soft X-ray band. Emission from the hot gas of temperature around 0.1–1 keV is often seen in the soft X-ray band. This hot gas is believed to be heated by shock fronts generated by supernova explosions and stellar winds (Persic et al. 2004).

Leveraging the 0.5'' resolution of *Chandra* ACIS, the Great Observatory All-sky LIRG Survey (GOALS) also studied the X-ray surface brightness distribution of U/LIRGs. Extended soft X-ray emission is clear even by visual inspection in most LIRGs. Most of GOALS U/LIRGs' soft X-ray emission, e.g., in the 0.5–2 keV band, spreads up to 2–10 kpc with a median value of 5.3 kpc (Iwasawa et al. 2011). A more compact, point-like hard X-ray emission is often found, e.g., within 1–3 kpc, in the GOALS sample. Exceptions were occasionally seen in a small number of objects where soft and hard X-ray emission regions are compact within a couple of kpc (Iwasawa et al. 2011).

In this work, we study an infrared galaxy pair Arp 302 in the X-ray band. A *Swift* ultraviolet image of Arp 302 (Arp 302N and Arp 302S) is shown in Fig. 1. Arp 302N is an edge-on galaxy and Arp 302S is a face-on galaxy (Armus et al. 2009). Arp 302 is a luminous infrared source with  $L_{\text{IR}} = 4.2 \times 10^{11} L_{\odot}$ . A burst of star formation usually explains the large infrared luminosity and almost all luminous infrared galaxies like Arp 302 are found to be rich in molecular gas (e.g. Sanders et al. 1991; Solomon et al. 1992). Interestingly, most of the star-forming activity in local LIRGs happens in a small region within a few kpc (Strickland & Heckman 2007). However, the CO emission extends over 23 kpc in Arp 302N and 10 kpc in Arp 302S, contrasting starbursts. Together with the low star-forming efficiency measured by  $L_{\text{IR}}/M(\text{H}_2)$ , Lo et al. (1997) concluded that the high infrared luminosity is not due to a high star-formation rate (SFR) but an unusual amount of molecular gas in Arp 302. Stars are forming a rate of only 1–4  $M_{\odot} \text{ yr}^{-1}$  in Arp 302 (Lo et al. 1997).

Joining the forces of *Spitzer*, *GALEX* and *HST* and *Chandra*, Armus et al. (2009) conducted a multi-wavelength study of Arp 302 as part of GOALS. The high infrared luminosity of the pair results from the enhanced infrared emission from Arp 302N alone. *Spitzer* found no or little evidence of significant Ne [v] emission from Arp 302S, indicating no significant AGN activity in the southern galaxy of the pair. The Ne [v]/Ne [III] and O [IV]/Ne [III] line ratios of Arp 302N measured by *Spitzer* indicates the presence of a weak AGN but contributing no more than 10–15% of the infrared luminosity of Arp 302N, based on the scaling of local AGNs and starburst nuclei (Armus et al. 2007). A preliminary look at the *Chandra* observation of Arp 302 found that Arp 302N shows significant X-ray emission, and AGN may dominate the hard X-ray emission band (Armus et al. 2009). Arp 302, consisting of two different types of galaxies within a gas-rich environment, is an excellent laboratory of a pair of interacting galaxies evolving along different paths.

In this paper, we re-analyse the *Chandra* observation and conduct detailed spectral analysis and X-ray surface brightness study to search for extended X-ray emission by including another *XMM-Newton* observation of Arp 302 in the archive. We aim to search for AGN X-ray activity in this infrared-luminous galaxy pair and investigate whether the measured soft X-ray luminosity is consistent with the SFR measurements at longer wavelengths. If the AGN activity is evident, we intend to identify the X-ray nature of the line-of-sight absorption, e.g., Compton-thin or Compton-thick, and study how its intrinsic X-ray luminosity compares to a typical Seyfert AGN.

The paper is organised in the following way: section 2 introduces our data reduction processes; section 3 presents an X-ray

surface brightness study based on the *Chandra* observation; section 4 demonstrates the baseline model for the X-ray emission from Arp 302N; we discuss our results in section 5.

## 2 DATA REDUCTION

### 2.1 *Chandra*

The information of the two X-ray observations of Arp 302 is in Tab 1. During the *Chandra* observation, the Advanced CCD Imaging Spectrometer (ACIS) was operated in the ACIS-S mode. Our data reduction for the *Chandra* observation was performed using CIAO v.4.15 and the calibration version 4.10.2 released on 15 November 2022. We reprocessed the data and extracted clean event lists using the `chandra_repro` routine. We then extracted spectra using the `SPEXTRACT` tool in CIAO. We specifically requested `correctpsf=yes` in `SPEXTRACT`, and then the location is passed into the `ARFCORR` task. So, the X-ray count rates, especially those in Section 3, have been corrected using the proper point spread functions. ACIS achieves a net count rate of  $0.0169 \pm 0.0011 \text{ cts s}^{-1}$ , which is significantly lower than the count rate threshold for pile-up effects.

In this work, we focus on the galaxy Arp 302N of the pair, which is brighter than the other galaxy in the X-ray band. The source spectrum of Arp 302N was extracted from a circle of 20 arcsec centred at the centre of the galaxy. The background spectrum was extracted from a nearby, source-free circle of 60 arcsec. The spectrum is grouped using `GRPPHA` to have a minimum count of 20 per bin.

### 2.2 *XMM-Newton*

We processed the *XMM-Newton* observation of Arp 302 using SAS v. 20.0 and the calibration version updated on 25 October 2022.

#### 2.2.1 *EPIC*

The EPIC observations were operated in the Full Frame mode. We extracted a clean event list using the `EMPROC` and `EPPROC` tools respectively for MOS and pn observations. Good time intervals (GTIs) were selected by removing flaring particle background-dominated intervals, defined as periods when the single event (`PATTERN=0`) count rate in the >10 keV band is higher than  $0.35 \text{ cts s}^{-1}$  for MOS data and that in the 10–12 keV band higher than  $0.4 \text{ cts s}^{-1}$  for pn data. We extracted the source spectra from a circular region of 20 arcsec and the background spectra from a nearby, source-free region of 100 arcsec. Next, we used the `RMFGEN` and `ARFGEN` tools to create redistribution matrix files and auxiliary files. We group the spectra using `GRPPHA` to have a minimum count of 20 per bin. The net pn, MOS1 and MOS2 count rates of Arp 302N during our observation are  $0.0399 \pm 0.0018$ ,  $0.0099 \pm 0.0008$  and  $0.0107 \pm 0.0008 \text{ cts s}^{-1}$ . They are lower than the X-ray count rate thresholds for the full-frame mode to have significant pile-up effects.

#### 2.2.2 *OM*

The study of the UV and optical emission of Arp 302N is beyond the purpose of this work. Therefore, we show a UVW1 image of Arp 302N in Fig. 1 only for comparison with the X-ray emission region. The exposure of this image is 1 ks. The image was extracted using the imaging mode data process tool `OMICHAIN`.

Mission	ObsID	Date	Length
<i>XMM-Newton</i>	0670300101	2012-01-16	29 ks
<i>Chandra</i>	7812	2006-12-17	15 ks

**Table 1.** The *XMM-Newton* and *Chandra* observations analysed in this work.

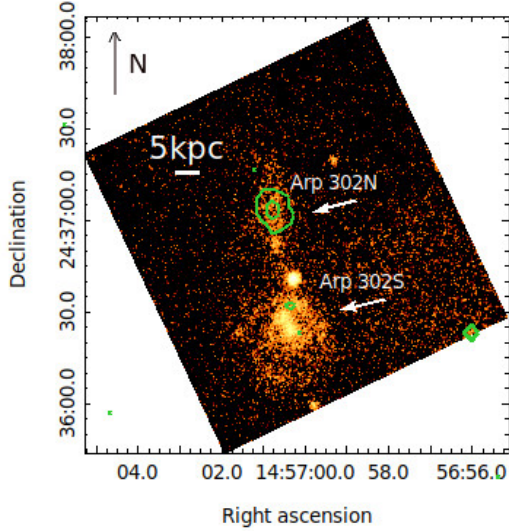


**Figure 1.** The OM image of the merging galaxies Arp 302 in the UVW1 band overlaid with ACIS X-ray contours (0.2 and 0.6 counts per pixel). We find significant evidence of X-ray emission from Arp 302N and some from Arp 302S. The position angle of the edge-on galaxy Arp 302N is north-south.

### 3 X-RAY FLUX SPATIAL DISTRIBUTION

Fig. 1 shows an OM image of Arp 302 in the UVW1 band. Two galaxies, marked by Arp 302N and Arp 302S, are clearly shown in the image. Two galaxies are separated by approximately 40 arcsec, which is around 26 kpc at the distance<sup>1</sup> of the Arp 302 (694 pc per arcsec at  $z = 0.033$ ). The relatively large separation suggests that Arp 302 is in an early phase of merging/interacting.

The green contours in Fig. 1 show the X-ray emission from Arp 302 measured by ACIS on *Chandra*. Some evidence of X-ray emission is found in Arp 302S. Most X-ray emissions originate in Arp 302N. The peak of the X-ray flux coincides with the centre of the galaxy. In this work, we focus on studying Arp 302N.

To further study the spatial distribution, we extract net X-ray count rate distribution for Arp 302N in 2–10 keV and 0.3–2 keV bands (see Fig. 2). The background counts have been extracted using the same background region in Section 2. Thanks to the arcsec resolution of ACIS, we find that most hard X-ray emission comes from a compact region of 3 arcsec (around 2 kpc). The soft X-ray emission region is more extended (up to 18 arcsec, around 12 kpc).

By modelling the distributions with Gaussian models, we obtain  $\sigma < 2.4$  kpc of the hard X-ray emission region, which suggests most hard X-ray emission comes from close to the central nuclear region. Two Gaussian models are required to fit the soft X-ray distribution, one with  $\sigma = 2.1 \pm 0.4$  kpc and the other with  $\sigma = 6.0^{+1.6}_{-1.2}$  kpc. The two Gaussian distributions may suggest two distinct compo-

<sup>1</sup> We assume  $H_0 = 67.8 \text{ km s}^{-1} \text{ Mpc}^{-1}$ ,  $\Omega_{\text{matter}} = 0.308$ ,  $\Omega_{\text{vacuum}} = 0.692$ .

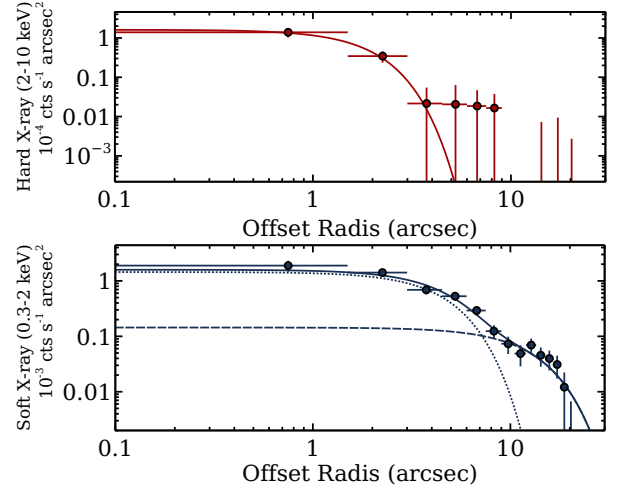


**Figure 2.** X-ray surface brightness of Arp 302N measured by ACIS. The centre is chosen to be the peak of the X-ray flux. The solid lines show the best-fit Gaussian distributions. The hard X-ray emission comes from a compact region with a radius of  $\sigma < 3.5$  arcsec (around 2 kpc). The soft X-ray emission region is consistent with two Gaussian distributions of  $\sigma = 3.1 \pm 0.6$  arcsec (around 2 kpc) and  $\sigma = 8.7^{+2.3}_{-1.7}$  arcsec (around 6 kpc).

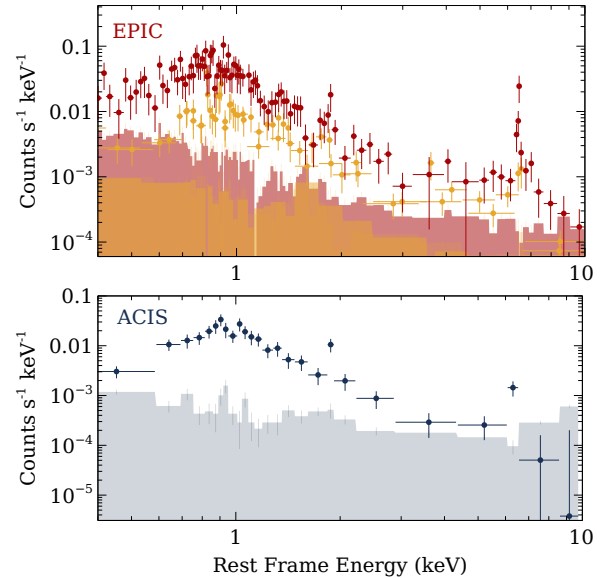


**Figure 3.** Source (crosses) and background spectra (shaded regions) of Arp 302N obtained by *XMM-Newton* (Red: pn; orange: MOS1 and MOS2) and *Chandra* (black: ACIS).

nents in the 0.3–2 keV band. We will discuss the soft X-ray spectral component of Arp 302N in the rest of the paper. The inner soft X-ray emission region has a similar size of a couple of kilo-parsec as the hard X-ray emission region. The outer soft X-ray emission region extends to more than 10 kpc.

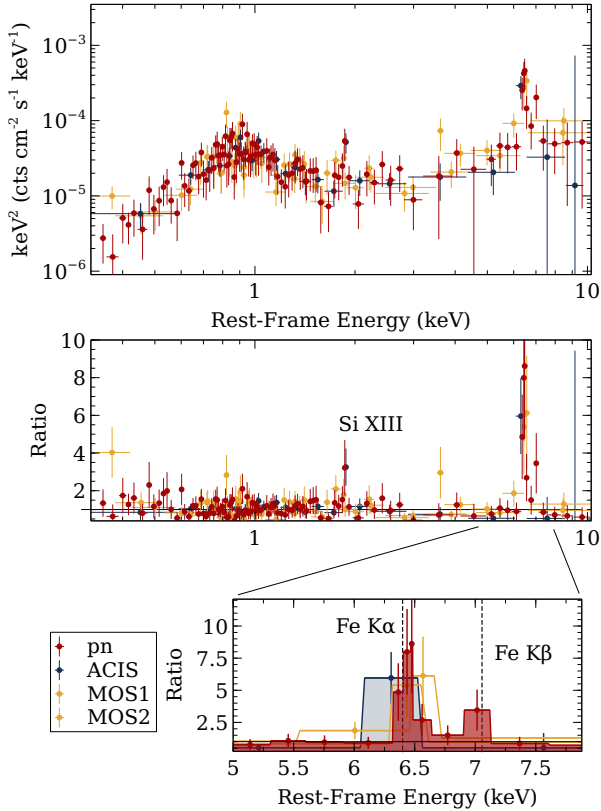


**Figure 4.** Top: folded spectra of Arp 302N but corrected for the effective area only for illustration purposes. Middle: data/model ratio plots for all four X-ray spectra using an absorbed continuum model including `zpower1w` and `mekal`. We find evidence of Fe K $\alpha$ , Fe K $\beta$  and Si XIII emission lines. Bottom: a zoom-in of the ratio plot in the iron emission band. The two vertical dashed lines mark the rest-frame energies of Fe K $\alpha$  (6.4 keV) and K $\beta$  (7.06 keV) emission.

## 4 SPECTRAL ANALYSIS

### 4.1 Continuum Modelling

We start the spectral analysis with continuum modelling. Fig. 3 and 4 show an overview of the *Chandra* and *XMM-Newton* spectra of Arp 302N.

In the soft X-ray band, we model the hot gas emission using the `mekal` model in XSPEC. The `mekal` model calculates X-ray spectra from optically thin gas (Mewe et al. 1985, 1986; Liedahl et al. 1995; Arnaud & Rothenflug 1985; Arnaud & Raymond 1992), e.g., in the star-forming region. We use the solar abundances calculated in Wilms et al. (2000) in the `mekal` model<sup>2</sup>. The free parameters of `mekal` are the temperature of the gas  $kT$  and the normalisation. Moreover, we follow the indication in Armus et al. (2009), which shows similar spectral shapes as Fig. 4, by modelling the hard X-ray emission using the `zpower1w` model. This power-law emission originates from the innermost accretion region of the AGN. The redshift parameters of `zpower1w` and `mekal` are fixed at the source redshift. We also consider different line-of-sight absorption column densities for the `mekal` and `zpower1w` models because they orig-

<sup>2</sup> In Wilms et al. (2000),  $Z_{\text{O,Fe}}/Z_{\text{O,H}}$  equals  $2.69 \times 10^{-5}$  and  $Z_{\text{O,Si}}/Z_{\text{O,H}}$  equals  $1.86 \times 10^{-5}$ . The silicon and iron abundances will be discussed in later sections

inate in two regions of the galaxy. The `ztbabs` model is used for this purpose. The redshift parameter of `ztbabs` is also fixed at the source redshift.

The `ztbabs` model is also used to account for Galactic absorption. Willingale et al. (2013) calculates the mean hydrogen column density  $N_{\text{H,Gal}} = N_{\text{HI}} + N_{\text{H}_2} = 3.56 \times 10^{20} \text{ cm}^{-2}$  in the direction of Arp 302N. Our X-ray data can not constrain the Galactic column density. This parameter is, therefore, fixed at this value. All `ztbabs` models consider the same abundances in Wilms et al. (2000). An additional constant is used to account for cross-calibration uncertainty between different instruments and epochs. The constant value of `pn` is fixed at 1. The relative values for the other three spectra are `MOS1/pn` =  $0.97 \pm 0.12$ , `MOS2/pn` =  $0.97 \pm 0.13$ , `ACIS/pn` =  $1.03 \pm 0.14$ . They are all consistent with the calibration uncertainty (Madsen et al. 2015). These values are independent of the choice of the model. The `ACIS/pn` ratio is consistent with 1, suggesting no significant X-ray luminosity change in two observations separated by five years.

In summary, the total continuum model is `constant * ztbabs * ( ztbabs1*mekal + ztbabs2*zpower1w )` in XSPEC notations. This model describes the continuum emission of Arp 302N very well. Fig. 4 shows the residuals in the continuum fitting. Three narrow emission lines are shown at 1.8, 6.4 and 7 keV of the data. These three features are also shown in the folded spectra Fig. 3 and the top panel of Fig. 4. The 1.8 keV emission feature was also shown in Fig. 7 in Armus et al. (2009) where the same *Chandra* spectrum was considered. We will analyse these three emission lines and estimate their significance in a later section.

### 4.2 The Metal Abundances of the Star-Forming Region

The underabundance of Fe relative to  $\alpha$  elements was found in nearby starbursts and local luminous infrared galaxies (Strickland et al. 2004; Grimes et al. 2005; Iwasawa et al. 2011). Some may be related to the enhanced production  $\alpha$  elements in Type II SN (Martin et al. 2002) or iron depletion in the boundary layer between the cold interstellar medium and SN winds (Strickland et al. 2004).

The CCD-resolution data of Arp 302N do not allow us to constrain the absolute abundances of elements in the `mekal` component. But by varying the iron abundance parameter while keeping a solar oxygen abundance, we may shed some light on the iron abundances in the star-forming region of Arp 302N. Because the  $Z_{\text{Fe}}/Z_{\text{O}}$  value determines the Fe L/ O K emission ratio in the soft X-ray band.

In Fig. 5, we show the measurement uncertainty of  $Z_{\text{Fe}}/Z_{\text{O}}$  and  $kT$  of the `mekal` model. There is clear evidence of degeneracy between the two parameters. Within the  $1 - \sigma$  uncertainty range, a model with  $Z_{\text{Fe}} = 0.4Z_{\text{O}}$  and  $kT=0.5$  keV can also explain the data. We, therefore, conclude that we cannot constrain the metal abundances of the hot gas of the star-forming region in Arp 302N. Although we measure the gas temperature by fixing the  $Z_{\text{Fe}}$  parameter of the `mekal` at solar in the following analysis, we note that a higher gas temperature is also possible if the metal abundances are lower.

### 4.3 Detection of Narrow Emission Lines

We fit the narrow emission lines shown in Fig. 4 with Gaussian line models `zgauss` in XSPEC. The redshift parameter is fixed at the source redshift. The best-fit parameters are shown in Table 2. The rest-frame energies of the three lines are  $6.44 \pm 0.04$ ,  $6.99 \pm 0.13$  and  $1.85 \pm 0.04$  keV, which align with the energies of Fe K $\alpha$ , Fe

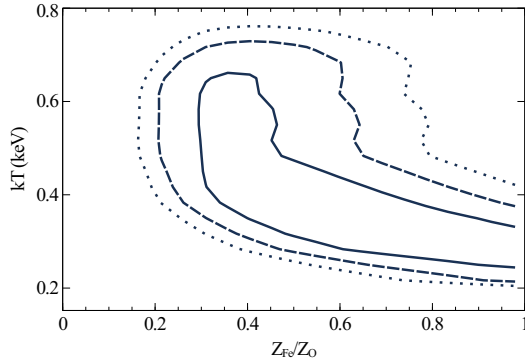


**Figure 5.**  $\chi^2$  distribution on the relative iron abundance  $Z_{\text{Fe}}/Z_{\text{O}}$  and the temperature of the gas. There is a degeneracy between these two parameters. The solid dashed and dotted curves show the 1, 2, 3- $\sigma$  uncertainty ranges.

$K\beta$  and Si XIII emission lines. Adding a Gaussian line model to fit each line decreases  $\chi^2$  by 67.64, 17.31 and 10.55, respectively. Each Gaussian line model introduces two extra free parameters, energy and normalisation. The line width of the three line models is fixed at a small value  $\sigma = 10^{-3}$  keV. If we free this parameter, we only obtain an upper limit<sup>3</sup> of  $\sigma < 0.1$  keV (90% confidence level). We, therefore, fix this parameter in the model.

To estimate the significance of the lines, we conduct a null hypothesis test by simulating 1000 sets of spectral simulations. The same exposure time as in the archival MOS1, MOS2, pn and ACIS observations is considered. The simulation model assumes no additional lines at 6.44, 6.99 and 1.85 keV. Only the best-fit continuum model shown in Table 2 (`constant * ztbabs * (ztbabs1*mekal + ztbabs2*zpowerlw)`) is used. We then search for emission line features by adding `zgauss` models with variable energy and normalisation parameters in the 1–3 keV and 5–10 keV and use the decrease of  $\chi^2$  as an indication of goodness-of-fit improvement. The distribution of  $\Delta\chi^2$  is shown in Fig. 7. 138 out of 1000 simulations have  $\Delta\chi^2 > 10.55$  by adding a Gaussian line in the 1–3 keV band of the simulated spectrum. We, therefore, estimate the significance of the 1.86 keV emission line to be 1-138/1000=86.2%. Similarly, the significance of the 6.99 keV line is 98.6%. No simulations have  $\Delta\chi^2$  higher than 67.64 as for the observed Fe  $K\alpha$  emission lines.

Narrow Fe  $K\alpha$  emission lines are commonly seen in luminous infrared galaxies. AGN and star-forming regions, e.g., from high-mass X-ray binaries (HMXBs) (e.g., Mineo et al. 2012), may contribute to the observed Fe  $K\alpha$  emission line. Based on the best-fit Gaussian line model in Table 2, we estimate the flux of the Fe  $K\alpha$  in Arp 302N is  $2.5 \times 10^{-14}$  erg cm<sup>-2</sup> s<sup>-1</sup>, corresponding to a line luminosity of  $7 \times 10^{40}$  erg s<sup>-1</sup>. Based on the Fe  $K\alpha$  line luminosity vs SFR relation compiled from observations of local luminous infrared galaxies ( $L_{\text{Fe}K\alpha}^{\text{HMXB}}$  (erg s<sup>-1</sup>) =  $(1.3 \pm 0.4) \times 10^{37}$  SFR ( $M_{\odot}$  yr<sup>-1</sup>), Pereira-Santaella et al. 2011), the strong Fe  $K\alpha$  line in Arp 302N would suggest a very high SFR of 5400  $M_{\odot}$  yr<sup>-1</sup>, if the star-forming region dominates the Fe  $K\alpha$  emission in Arp 302N. This conflicts with the study in the millimeter-wave observations of Arp 302N (e.g., SFR=1-4  $M_{\odot}$  yr<sup>-1</sup>, Lo et al. 1997). We conclude that the Fe  $K\alpha$  emission line originates in the AGN rather than the galaxy’s star-forming region.

<sup>3</sup> This upper limit corresponds to FWHM<0.236 keV. For the 6.44 keV line, the velocity dispersion is smaller than  $v < 0.236/6.4c = 0.04c$ .

Models	Parameters	Units	Model 0
ztbabs1	$N_{\text{H},1}$	$10^{21}$ cm <sup>-2</sup>	$6.0^{+1.3}_{-1.4}$
mekal	$kT$	keV	$0.23^{+0.06}_{-0.02}$
	$Z_{\text{Si}}$	$Z_{\odot}$	1 (f)
	Norm1	$10^{-4}$	$5^{+4}_{-3}$
ztbabs2	$N_{\text{H},2}$	$10^{20}$ cm <sup>-2</sup>	< 5
zpowerlw	$\Gamma$	-	$1.4 \pm 0.2$
	Norm2	$10^{-6}$	$8.3 \pm 0.7$
zgauss	Eline1	keV	$6.44 \pm 0.04$
	EW	eV	$3369^{+24}_{-52}$
zgauss	Eline2	keV	$6.99 \pm 0.13$
	EW	eV	$1125^{+14}_{-27}$
zgauss	Eline3	keV	$1.86 \pm 0.04$
	EW	eV	$137^{+24}_{-13}$
	$\chi^2/\nu$	-	192.47/196

**Table 2.** A simple phenomenological model (Model 0) for the 0.5–10 keV spectra of Arp 302N. The 2-10 keV luminosity of the power-law component (`zpowerlw`) is  $10^{41}$  erg s<sup>-1</sup> based on the best-fit unabsorbed flux. This value is significantly lower than the expected X-ray luminosity by given measured infrared spectral measurements of the AGN in Arp 302N using the scaling factors in (Spinoglio et al. 2022). See text for more details.

#### 4.4 A Torus Model of the Obscured Power-Law Emission and Fe K Emission Lines

In Model 0, we only obtain an upper limit for the line-of-sight column density of the power-law component (`zpowerlw`),  $< 5 \times 10^{20}$  cm<sup>-2</sup>. The little absorption in the continuum emission and the significant evidence of strong Fe K emission lines (equivalent width of >3000 eV for Fe  $K\alpha$  and >1000 eV for Fe  $K\beta$ ) forces us to re-evaluate the origin of the X-ray continuum emission.

More specifically, one can estimate the expected X-ray luminosity of Arp 302N by scaling the infrared measurements of the same object using statistical correlations drawn from a large sample of galaxies. Armus et al. (2009) measured the Ne [v] (14.3  $\mu\text{m}$ ), Ne [v] (24.3  $\mu\text{m}$ ) and O [iv] (25.9  $\mu\text{m}$ ) line flux of Arp 302N to be 1.2, 2.3 and  $12.3 \times 10^{-17}$  W m<sup>-2</sup> using *Spitzer*. Using the relation compiled from one hundred nearby infrared galaxies in Fig.1–3 of Spinoglio et al. (2022), we expect the 2–10 keV luminosity of Arp 302N to be around  $10^{43}$  erg s<sup>-1</sup>, which is 100 times higher than the value of the best-fit power-law component in Model 0 ( $10^{41}$  erg s<sup>-1</sup> in the 2–10 keV band calculated using the best-fit unabsorbed flux).

In this section, we explored the possible evidence of a heavily obscured power-law component in our spectral data below 10 keV. The observed power-law component with little absorption in Model 0 may, instead, originate in scattering materials as seen in most Seyfert 2 AGN (e.g., Turner et al. 1997) rather than direct emission from the hot corona.

##### 4.4.1 Model Set-Up

Following the indications of previous work on obscured AGNs in LIRGs (e.g., Yamada et al. 2021; Laloux et al. 2022), we explain the Fe  $K\alpha$  and  $K\beta$  emission lines consistently with a torus model of gas and dust surrounding the AGN as in a typical Seyfert 2 AGN (Antonucci 1984). We adopted the mytorus model (Murphy & Yaqoob 2009), where the covering factor of a toroidal-shaped torus is fixed at 0.5. The full model is `constant *`

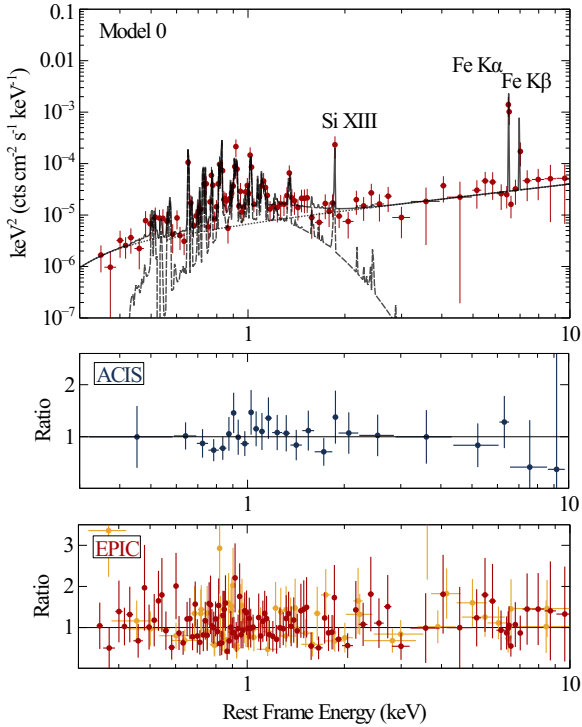


**Figure 6.** The best-fit Model 0 for the X-ray spectra of Arp 302N overlaid with the unfolded pn spectrum. Solid line: total model; dashed line: `mekal1`. The detected emission lines in Fig. 4 are modelled by Gaussian lines. The bottom two panels show corresponding data/model ratio plots.

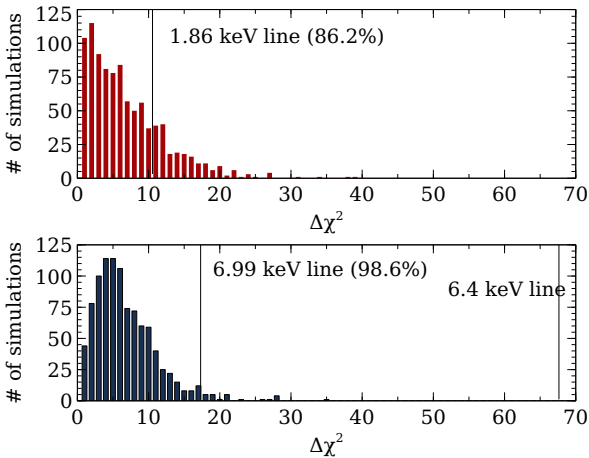


**Figure 7.**  $\chi^2$  improvement by adding an additional Gaussian line in the 1–3 keV and 5–10 keV bands in 1000 simulations. See text for more details. 138/1000 simulations have  $\Delta\chi^2 > 10.55$  in the 1–3 keV band and 14/1000 simulations have  $\Delta\chi^2 > 17.31$  in the 5–10 keV band. The confidence of positive detection of Si XIII (1.86 keV) and Fe XXVI (6.95 keV) is respectively 86.2% and 98.6%.

`ztbabs * (ztbabs1*mekal + trans.obs * zpowerlw1 + scattered.con + fluor.lines + zpowerlw2)` (Model T) in XSPEC notation. We used the coupled mode of the `mytorus` model, so the scaling factors of the Compton-scattered continuum emission (`scattered.con`) and fluorescent line emission (`fluor.lines`) are linked. Due to the lack of hard X-ray data, there is a degeneracy between the line-of-sight column density and the strength of the

Models	Parameters	Units	Values
<code>ztbabs1</code>	$N_{H,1}$	$10^{21} \text{ cm}^{-2}$	$7.4^{+0.4}_{-0.3}$
<code>mekal1</code>	$kT_1$	keV	$0.30 \pm 0.03$
	$Z_{\text{Si}}$	$Z_{\odot}$	$8 \pm 3$
	Norm1	$10^{-4}$	$2.7^{+1.8}_{-0.3}$
<code>mytorus</code>	$\log(N_{H,2})$	$\text{cm}^{-2}$	$> 3 \times 10^{24}$
<code>reprocessed</code>	$Z_{\text{Fe}}$	$Z_{\odot}$	1(f)
	Norm2	$10^{-5}$	$91^{+3}_{-2}$
<code>obscured</code>	$N_{H,3}$	$\text{cm}^{-2}$	$= N_{H,2}$
<code>zpowerlw1</code>	$\Gamma_1$	-	$= \Gamma_1$
	Norm3	$10^{-5}$	$= \text{Norm2}$
<code>scattered</code>	$\Gamma_2$	-	$1.78^{+0.08}_{-0.09}$
<code>zpowerlw2</code>	Norm4	$10^{-5}$	$0.7 \pm 0.2$
	$\chi^2/\nu$	-	201.06/200

**Table 3.** Model T adopts the `mytorus` model to calculate Fe emission lines by given gas column density. The `mytorus` model has three components: reprocessed emission (continuum emission and lines), obscured direct power-law emission, and unobscured scattered power-law emission.

obscured, direct power-law emission (`zpowerlw1`). We, therefore, link the line-of-sight column density with the average column density of the torus. Such a model would allow us to consistently calculate the emission from the torus and line-of-sight absorption by giving the same column density.

In addition, Model 0 suggests a modest column density along our line of sight towards the collisionally ionised gas component `mekal1` (around  $6 \times 10^{21} \text{ cm}^{-2}$ ). We, therefore, considered an independent line-of-sight absorption calculated by `ztbabs1` for the `mekal1` model. We also allowed a variable Silicon abundance in the `mekal1` model to fit the Si XIII emission line.

#### 4.4.2 Results

Model T provides the spectra of Arp 302N a good fit with  $\chi^2/\nu = 201.06/200$ . The best-fit parameters are shown in Table 3. Assuming the line-of-sight column density ( $N_{H,3}$ ) is the same as the average column density of the torus ( $N_{H,2}$ ), we find a lower limit of these two parameters in Model T. Fig. 9 shows  $\Delta\chi^2$  vs.  $N_{H,3,4}$ . The 90%-confidence lower limit is  $3 \times 10^{24} \text{ cm}^{-2}$ , indicating Compton-thick medium. Note that the maximum of the allowed column density values in the `mytorus` model is  $10^{25} \text{ cm}^{-2}$ . The scattering fraction of the continuum emission is  $\text{Norm4}/\text{Norm2} = 7 \times 10^{-6}/9 \times 10^{-4} = 0.8\%$ , consistent with the median value of known Sey2 AGN (Gupta et al. 2021). In addition, to fit the observed Si XIII emission, a super-solar silicon abundance of  $8Z_{\odot}$  is required for the `mekal1` model.

In summary, the observed unabsorbed power-law emission in Arp 302N is interpreted as the scattered emission from the circumnuclear materials in Model T. The direct power-law emission from the hot corona close to the SMBH is highly obscured in these models. This model explains the lack of obscuration in the power-law continuum emission (`zpowerlw1`) based on a model similar to the ones for typical Seyfert 2 AGN. They naturally suggest a higher intrinsic AGN luminosity than Model 0. See Section 5 for more discussion regarding the intrinsic AGN luminosity.

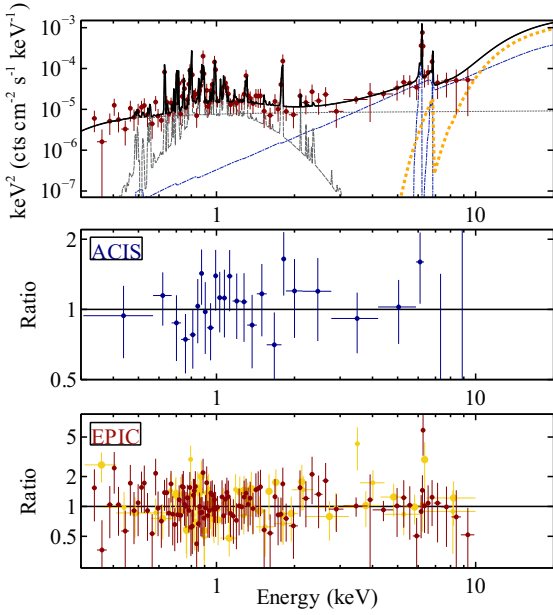


**Figure 8.** Top: best-fit mytorus models for the *XMM-Newton* and *Chandra* spectra of Arp 302N. Black solid line: total model; grey dashed line: unobscured, scattered power-law emission; blue dash-dotted lines: Compton-scattered continuum and line emission components; orange dotted lines: obscured power-law components. The red crosses are the unfolded pn spectrum of Arp 302N. Middle: corresponding *Chandra* data/model ratio plot. Bottom: the same data/model ratio but for *XMM-Newton* spectra (red: pn; yellow: MOS1 and 2).

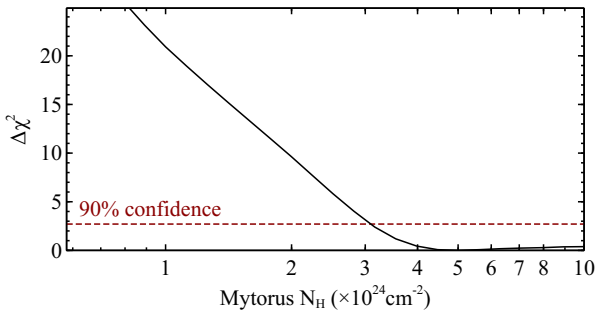


**Figure 9.**  $\Delta\chi^2$  vs. the hydrogen column density of the torus in the mytorus model (Model T). The dashed line shows the 90%-confidence lower limit is  $3 \times 10^{24} \text{ cm}^{-2}$ .

## 5 DISCUSSION

### 5.1 An X-ray view of the star-forming region in Arp 302N

By analysing the soft X-ray surface brightness of Arp 302N measured by *Chandra*, we find that the soft X-ray emission of Arp 302N is consistent with two Gaussian distributions. The first component has a size of  $\sigma = 2 \text{ kpc}$ ; the second has a size of  $\sigma = 6 \text{ kpc}$ . The first component has a similar emission size as the hard X-ray emission, while *Chandra* detected significant emission in the second component up to 12 kpc.

Detailed spectral modelling suggests that AGN and star-forming regions contribute to the soft X-ray emission of Arp 302N, in agreement with the indication of two soft X-ray components in the image. The more extended soft X-ray emission found in the surface brightness study likely corresponds to the star-forming component

in the spectrum. We conclude that the size of the star-forming region extends to at least 12 kpc in Arp 302N. It is worthwhile to mention that extended soft X-ray emission, e.g.,  $< 2 \text{ keV}$ , spreading up to 2–10 kpc is frequently found in other U/LIRGs, while hard X-ray emission, e.g., 2–10 keV, is more compact within 1–3 kpc (Iwasawa et al. 2011).

In addition to the soft X-ray emission region size in Arp 302N, we can also estimate the SFR of Arp 302N based on the relation between X-ray luminosity and SFR. Adapting the relation  $\text{SFR} \approx L_{2-10\text{keV}}/10^{39} M_{\odot} \text{ yr}^{-1}$  (Franceschini et al. 2003), we estimate the SFR of Arp 302N to be  $1-2 M_{\odot} \text{ yr}^{-1}$  based on the best-fit Model T. This value is similar to the estimation in Lo et al. (1997) based on  $L_{\text{IR}}/M(\text{H}_2)$ : Lo et al. (1997) argues that the high infrared luminosity of Arp 302N is not due to starbursts in the nuclear region, but its considerable amount of molecular gas, among which stars are forming at only  $\text{SFR}=1-4 M_{\odot} \text{ yr}^{-1}$ .

An intriguing result from our analysis is the evidence of the 1.86 keV emission line in both *XMM-Newton* and *Chandra* observations of Arp 302N separated by five years. Our confidence of a positive detection is around 86.2% estimated from simulations. This line energy corresponds to a Si XIII emission line. The diffuse gas in the star-forming region is the only explanation for this emission line in the soft X-ray band. A significant silicon overabundance of  $Z_{\text{Si}} = 8Z_{\odot}$  is required to explain the data. The super-solar silicon abundance might be related to the past core-collapse supernovae in Arp 302N. For example, an over-abundance of silicon has been found in the circumstellar medium of Galactic core-collapse supernova remnants (e.g. Bhalerao et al. 2019).

We explored the possibility of a second hot gas component (*mekal*), representing a separate star-forming region in Arp 302N, to explain the Si XIII emission line without the requirement for a super-solar silicon abundance. Such a model needed two *mekal* components of  $kT = 0.33$  and  $0.64 \text{ keV}$ . However, such a model would infer an overall X-ray luminosity of the star-forming region ten times higher than Model T, corresponding to an SFR of  $20 M_{\odot} \text{ yr}^{-1}$ . This value does not match observations at longer wavelength (Lo et al. 1997). We, therefore, exclude such a model.

The CCD-resolution data from *XMM-Newton* and *Chandra* cannot resolve the detailed spectral lines of the hot gas in the star-forming region, but future microcalorimeter-resolution data, e.g. from *Athena* (Nandra et al. 2013), will do. We show simulations of one X-IFU observation based on Model T. The evidence of the finest emission lines, such as C IV emission, will answer this question. *AXIS* (Mushotzky et al. 2019) is a future X-ray mission with CCD-resolution data but a much higher effective area than *Chandra*. Despite no detailed lines resolved in the soft X-ray band, e.g.,  $< 1 \text{ keV}$ , *AXIS* will still show a significant advantage in detecting Fe K $\alpha$  and K $\beta$  emission over *Chandra*.

### 5.2 The AGN activity in Arp 302N

Our *XMM-Newton* and *Chandra* spectra of Arp 302N show that a power-law component dominating the  $< 10 \text{ keV}$  band has little absorption. Assuming this power-law emission originates from the central accretion region of the AGN, e.g., the hot coronal region near the SMBH, we estimate the AGN of Arp 302N has a 2–10 keV luminosity of  $10^{41} \text{ erg s}^{-1}$ . This value contrasts the expected X-ray luminosity scaled by previous *Spitzer* measurement of the AGN activity in Arp 302N (Armus et al. 2009) using a scaling correlation between infrared neon and oxygen emission line luminosity and X-ray luminosity in Spinoglio et al. (2022). See Section 4.4 for more details.

We, therefore, proposed a model with a heavily obscured power-law emission in the data. Our analysis fits the AGN emission with the *mytorus* model following the indications of previous work on other obscured AGNs in LIRGs (e.g., [Yamada et al. 2021](#); [Laloux et al. 2022](#)). Such a model allows us to consistently calculate Fe K emission lines and photoelectric absorption by assuming the same value for the torus’s line-of-sight and average column density.

When both a direct, obscured power law and a scattered, unobscured power law are considered, the inferred intrinsic AGN X-ray luminosity of Arp 302N is higher in Model T than in Model 0. The resulting 2–10 keV unabsorbed luminosity of the power-law component is  $1.0 \times 10^{43} \text{ erg s}^{-1}$ . This value matches the expectation based on previous *Spitzer* measurements of the AGN activity of this galaxy ([Armus et al. 2009](#)). Assuming a BH mass of  $10^8 M_{\odot}$ , this luminosity corresponds to  $L_{2-10\text{keV}}/L_{\text{Edd}} = 10^{-3}$ . This value is reasonable for a typical Seyfert 2 AGN ([Bian & Gu 2007](#)). In addition, the scattering fraction of the power-law emission of Arp 302N is around 0.7% (Norm4/Norm2), similar to other Seyfert 2 AGNs ([Gupta et al. 2021](#)). Although no report yet on the optical classification of Arp 302N, e.g., from SDSS, Arp 302N might host a Seyfert 2 AGN where the X-ray emission from the accretion region is highly obscured.

A column density of at least  $3 \times 10^{24} \text{ cm}^{-2}$  is required to explain the apparent lack of obscured power-law emission below 10 keV and the evidence of significant Fe K emission lines, suggesting a Compton-thick environment in the AGN of Arp 302N. Our spectral analysis adds more supporting evidence of hidden AGN activity in the sample of early merging galaxies. The Compton-thick circumnuclear environment revealed by our X-ray spectral analysis provides a complementary view of the dust and gas in the LIRG Arp 302N.

Our best-fit torus model predicts a 14–195 keV flux of  $5.4 \times 10^{-12} \text{ erg cm}^{-2} \text{ s}^{-1}$  from Arp 302N, which is lower than the sensitivity of the Swift-BAT survey<sup>4</sup>. Due to the lack of hard X-ray data, we had to assume the line-of-sight column density and the average column density of the torus are identical in Model T. However, this assumption may not hold. For example, evidence of the clumpiness in the torus has been found in both X-ray and infrared observations (e.g., [Krolik & Begelman 1988](#); [Mason et al. 2009](#); [Laha et al. 2020](#); [Zhao et al. 2021](#)). Future high-sensitivity, hard X-ray missions like *HEX-P* ([Madsen et al. 2019](#)) will more precisely measure the obscured power-law component in the hard X-ray band of Arp 302N and test for different torus models. In Fig. 10, we show two simulations, one based on Model 0 without obscured power law-shaped AGN emission and one based on Model T with a full torus model. *HEX-P* will easily distinguish two models in the hard X-ray band. More relevant simulations for the *HEX-P* spectra of obscured AGN can be found in [Boorman et al. \(2023\)](#).

## 6 CONCLUSION

We present an analysis of the *Chandra* and *XMM-Newton* observations of the non-starburst, luminous infrared galaxy Arp 302N. Arp 302N is one of the two galaxies in Arp 302. The two galaxies are separated by 26 kpc, suggesting an early galaxy interaction/merging phase. Previous observations at longer wavelengths found that the high infrared luminosity of Arp 302N is not due to a high SFR but a

large amount of molecular gas spreading up to 23 kpc. By studying its X-ray emission, we made the following conclusions:

- *Chandra* detects significant soft X-ray emission (0.3–2 keV) up to 12 kpc in Arp 302N from the peak of the X-ray emission. By modelling the X-ray surface brightness, we find two Gaussian-like emission regions, one with  $\sigma=2.1 \pm 0.4$  kpc and the other with  $\sigma=6.0^{+1.6}_{-1.2}$  kpc. The smaller soft X-ray emission region has a similar size as the hard X-ray emission (2–10 keV).
- We detect significant Fe K $\alpha$  and Fe K $\beta$  (98.6% confidence) emission lines from Arp 302N. We explore the possibility of consistently explaining the Fe K emission lines and line-of-sight absorption by given column density. Such a model suggests that a Compton-thick circumnuclear environment with  $N_{\text{H}} > 3 \times 10^{24} \text{ cm}^{-2}$ . Future hard X-ray telescopes, such as *HEX-P*, will be able to more precisely measure the torus geometry, test for clumpiness in the torus and determine its hard X-ray luminosity.
- Our best-fit X-ray model suggests an intrinsic X-ray (2–10 keV) luminosity of  $10^{43} \text{ erg s}^{-1}$ , consistent with the previous *Spitzer* measurements of the AGN activity in Arp 302N ([Armus et al. 2009](#)). The unobscured power-law emission with a luminosity of  $10^{41} \text{ erg s}^{-1}$  that dominates the <10 keV band is the Thomson scattered emission from the distant Compton-thin circumnuclear materials. The scattering fraction is 0.7% in Arp 302N. The line-of-sight column density, scattering fraction and intrinsic X-ray luminosity suggests a Seyfert 2-like AGN in Arp 302N. Future optical spectral observations will provide further confirmation of the AGN classification.
- Both the unobscured, scattered power-law emission and the hot gas in the star-forming region in Arp 302N contribute to the soft X-ray emission of Arp 302N. We estimate Arp 302N has  $\text{SFR}=1 - 2 M_{\odot} \text{ yr}^{-1}$  using the X-ray luminosity of the hot gas in the star-forming region. This result matches previous CO measurements at longer wavelengths ([Lo et al. 1997](#)).
- We detect a Si XIII emission line in the ACIS and pn spectra of Arp 302N (86.2% confidence). It can be explained by the super-solar silicon abundance of the hot gas in the star-forming region and associated with past core-collapse supernovae in Arp 302N. Similar silicon enrichment was observed in the circumstellar medium of Galactic supernova remnants. Future high-resolution X-ray spectral data, e.g., from *Athena*, will uniquely probe the ionisation state and metallicity of the hot gas in the star-forming regions in the LIRGs with obscured AGNs.

## ACKNOWLEDGEMENTS

J.J. acknowledges support from the Leverhulme Trust, the Isaac Newton Trust and St Edmund’s College, University of Cambridge. W.B. acknowledge support by the Science and Technology Facilities Council. We acknowledge the valuable discussion on plasma modelling with Timothy R. Kallman and Honghui Liu.

## DATA AVAILABILITY

The *XMM-Newton* and *Chandra* data are available for download at <https://heasarc.gsfc.nasa.gov>. The *mytorus* model is available at <https://www.mytorus.com>. No new data or models were produced in this work.

<sup>4</sup> The 105-month Swift-BAT survey is a uniform hard X-ray all-sky survey with a sensitivity of  $8.4 \times 10^{-12} \text{ erg cm}^{-2} \text{ s}^{-1}$  over 90% of the sky in the 14–195 keV band ([Oh et al. 2018](#)).



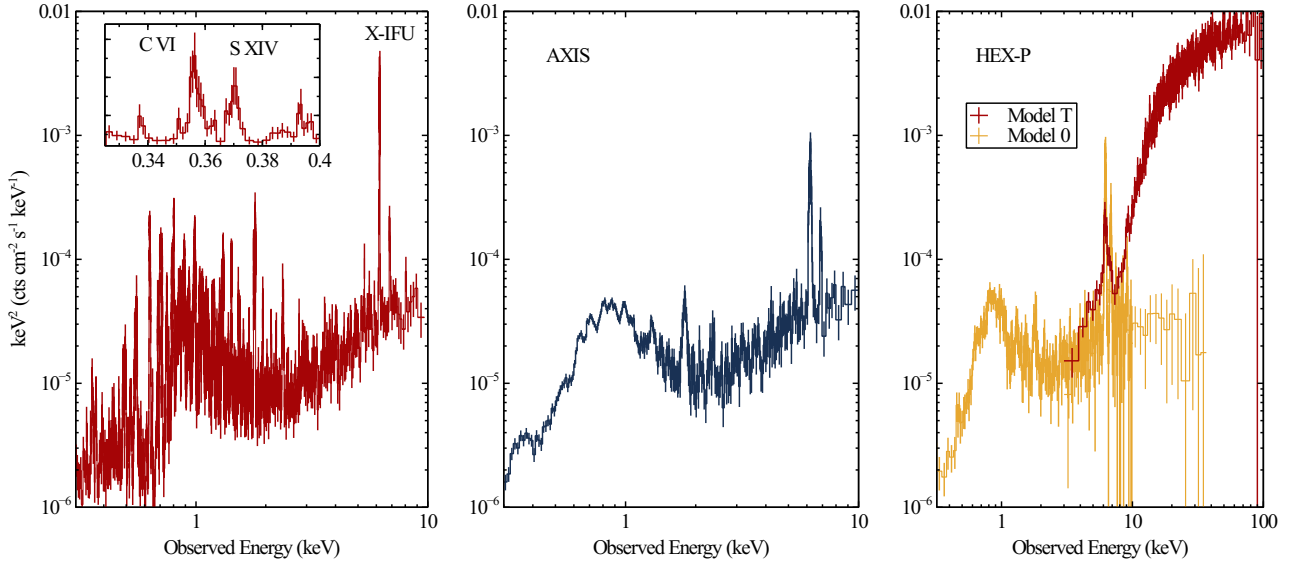


**Figure 10.** Simulated *Athena* X-IFU, *AXIS* and *HEX-P* spectra of Arp 302N using Model T. An exposure of 100 ks is considered for all three simulations. Left: the evidence of ionised emission lines, such as C  $\nu$ , holds the answer to the origin of the soft X-ray emission below 0.7 keV in Arp 302N. *Athena* will provide an unprecedented constraint on these emission lines. Middle: *AXIS* has a CCD resolution detector. Although it cannot resolve all the emission lines in the soft X-ray band, it shows significant improvement in measuring the Fe K $\alpha$  and Fe K $\beta$  emission of the photoionised gas compared to *Chandra*. It is important to note the arcsecond angular resolution of *AXIS*. Combined with the high effective area, *AXIS* will more precisely measure the surface brightness of Arp 302N in X-rays. Right: *HEX-P* will provide an important view of the hard X-ray emission from Arp 302N. Future hard X-ray observations will provide direct evidence of an obscured AGN in Arp 302N, based on which we can study the accretion state of the AGN, e.g., a low-luminosity AGN or a typical Seyfert 2 AGN. A simulated low-energy detector spectrum based on only Model 0 is shown in this panel for clarity.

## REFERENCES

- Antonucci R. R. J., 1984, *ApJ*, **278**, 499
- Armus L., et al., 2007, *The Astrophysical Journal*, **656**, 148
- Armus L., et al., 2009, *PASP*, **121**, 559
- Arnaud M., Raymond J., 1992, *ApJ*, **398**, 394
- Arnaud M., Rothenflug R., 1985, *A&AS*, **60**, 425
- Bhalerao J., Park S., Schenck A., Post S., Hughes J. P., 2019, *ApJ*, **872**, 31
- Bian W., Gu Q., 2007, *ApJ*, **657**, 159
- Boorman P. G., et al., 2023, *arXiv e-prints*, p. arXiv:2311.04949
- Clements D. L., Sutherland W. J., McMahon R. G., Saunders W., 1996, *MNRAS*, **279**, 477
- Efstathiou A., et al., 2022, *MNRAS*, **512**, 5183
- Franceschini A., et al., 2003, *MNRAS*, **343**, 1181
- Grimes J. P., Heckman T., Strickland D., Ptak A., 2005, *ApJ*, **628**, 187
- Gupta K. K., et al., 2021, *MNRAS*, **504**, 428
- Hopkins P. F., Somerville R. S., Hernquist L., Cox T. J., Robertson B., Li Y., 2006, *ApJ*, **652**, 864
- Iwasawa K., et al., 2011, *A&A*, **529**, A106
- Kawaguchi T., Yutani N., Wada K., 2020, *ApJ*, **890**, 125
- Krolik J. H., Begelman M. C., 1988, *ApJ*, **329**, 702
- Laha S., Markowitz A. G., Krumpke M., Nikutta R., Rothschild R., Saha T., 2020, *ApJ*, **897**, 66
- Laloux B., et al., 2022, *Monthly Notices of the Royal Astronomical Society*, **518**, 2546
- Liao S., et al., 2023, *Monthly Notices of the Royal Astronomical Society*, **520**, 4463
- Liedahl D. A., Osterheld A. L., Goldstein W. H., 1995, *ApJ*, **438**, L115
- Lin C.-H., Chen K.-J., Hwang C.-Y., 2023, *The Astrophysical Journal*, **952**, 121
- Lo K. Y., Gao Y., Gruendl R. A., 1997, *ApJ*, **475**, L103
- Madsen K. K., et al., 2015, *ApJ*, **812**, 14
- Madsen K., et al., 2019, *Bulletin of the AAS*, **51**
- Martin C. L., Koblunick H. A., Heckman T. M., 2002, *ApJ*, **574**, 663
- Mason R. E., Levenson N. A., Shi Y., Packham C., Gorjian V., Cleary K., Rhee J., Werner M., 2009, *The Astrophysical Journal*, **693**, L136
- Mewe R., Gronenschild E. H. B. M., van den Oord G. H. J., 1985, *A&AS*, **62**, 197
- Mewe R., Lemen J. R., van den Oord G. H. J., 1986, *A&AS*, **65**, 511
- Mineo S., Gilfanov M., Sunyaev R., 2012, *Monthly Notices of the Royal Astronomical Society*, **419**, 2095
- Murphy K. D., Yaqoob T., 2009, *MNRAS*, **397**, 1549
- Mushotzky R., et al., 2019, in *Bulletin of the American Astronomical Society*, p. 107 (arXiv:1903.04083)
- Nandra K., et al., 2013, *arXiv e-prints*, p. arXiv:1306.2307
- Oh K., et al., 2018, *ApJS*, **235**, 4
- Pereira-Santaella M., et al., 2011, *A&A*, **535**, A93
- Pérez-Torres M., Mattila S., Alonso-Herrero A., Aalto S., Efstathiou A., 2021, *A&ARv*, **29**, 2
- Persic M., Rephaeli Y., Braito V., Cappi M., Della Ceca R., Franceschini A., Gruber D. E., 2004, *A&A*, **419**, 849
- Ricci C., et al., 2017, *MNRAS*, **468**, 1273
- Ricci C., et al., 2023, *arXiv e-prints*, p. arXiv:2311.01494
- Sanders D. B., Mirabel I. F., 1996, *ARA&A*, **34**, 749
- Sanders D. B., Scoville N. Z., Soifer B. T., 1991, *ApJ*, **370**, 158
- Solomon P. M., Downes D., Radford S. J. E., 1992, *ApJ*, **387**, L55
- Spinoglio L., Fernández-Ontiveros J. A., Malkan M. A., 2022, *The Astrophysical Journal*, **941**, 46
- Stierwalt S., et al., 2013, *ApJS*, **206**, 1
- Strickland D. K., Heckman T. M., 2007, *ApJ*, **658**, 258
- Strickland D. K., Heckman T. M., Colbert E. J. M., Hoopes C. G., Weaver K. A., 2004, *ApJS*, **151**, 193
- Turner T. J., George I. M., Nandra K., Mushotzky R. F., 1997, *ApJS*, **113**, 23
- Willingale R., Starling R. L. C., Beardmore A. P., Tanvir N. R., O’Brien P. T., 2013, *MNRAS*, **431**, 394
- Wilms J., Allen A., McCray R., 2000, *ApJ*, **542**, 914
- Yamada S., Ueda Y., Tanimoto A., Imanishi M., Toba Y., Ricci C., Privon G. C., 2021, *ApJS*, **257**, 61
- Yuan T. T., Kewley L. J., Sanders D. B., 2010, *ApJ*, **709**, 884
- Zhao X., Marchesi S., Ajello M., Cole D., Hu Z., Silver R., Torres-Albà N., 2021, *A&A*, **650**, A57

